

# Generation of Perfect Vortex Beams by Dielectric Geometric Metasurface for Visible Light.

Qianwei Zhou<sup>1,2</sup>, Mingze Liu<sup>1,2</sup>, Wenqi Zhu<sup>3,4</sup>, Lu Chen<sup>3,4</sup>, Yongze Ren<sup>1,2</sup>, Henri J. Lezec<sup>3</sup>, Yanqing Lu<sup>1,2</sup>, Amit Agrawal<sup>3,4</sup>, Ting Xu<sup>1,2</sup>

1. National Laboratory of Solid-State Microstructures, Jiangsu Key Laboratory of Artificial Functional Materials, College of Engineering and Applied Sciences, Nanjing University, Nanjing 210093, China
2. Collaborative Innovation Center of Advanced Microstructures, Nanjing 210093, China
3. Physical Measurement Laboratory, National Institute of Standards and Technology, Gaithersburg, Maryland 20899, United States
4. Maryland NanoCenter, University of Maryland, College Park, Maryland 20899, United States

**Perfect vortex beam (PVB) is a propagating optical field carrying orbital angular momentum (OAM) with a radial intensity profile that is independent of topological charge. PVB can be generated through the Fourier transform of a Bessel-Gaussian beam, which typically requires a well-aligned optical setup consisting of a spiral phase plate, an axicon, and a lens. Here, based on a single-layer dielectric metasurface, we demonstrate the broadband generation of PVBs across the entire visible spectrum. The metasurface is composed of TiO<sub>2</sub> nanopillars acting as deep-subwavelength half-waveplates, and able to provide the desired geometric phase profile to an incident circularly polarized light for the generation of PVBs. Through rigorous optimization of the nanopillars' structural parameters, we experimentally generate vortex beams carrying OAM with different topological charges that exhibit constant radial intensity profiles, verifying their "perfect" characteristics. Furthermore, we also demonstrate that the ellipticity and diameter of a PVB can be simultaneously controlled by adjusting the structural parameters of the metasurface, which further increases the flexibility in their design. These results open a new route towards creating ultra-compact, flat, multifunctional nanophotonic platforms for efficient generation of structured light beams.**

## 1. Introduction

Vortex is a common physical phenomenon that occurs in nature such as during a typhoon and in oceanic currents. Equivalently, the concept of the vortex also exists in the field of optics where an optical vortex beam is characterized by a helical wavefront and a spatial phase dependence factor  $e^{il\varphi}$ , where  $l$  is an integer and denotes the topological charge and  $\varphi$  is the angular coordinate<sup>1,2</sup>. As a result, an optical vortex beam carries orbital angular momentum (OAM) and has a doughnut-shaped transverse intensity profile. Although vortex beams have been widely adopted for various optical applications such as quantum information processing<sup>3,4</sup>, optical trapping<sup>5-7</sup>, and particle manipulation<sup>8,9</sup>, the diameter of their annular intensity profile depends on the value of topological charge, which makes them non-ideal for applications requiring spatial superposition of vortex beams with different topological charges<sup>10</sup>. In this context, the concept of perfect vortex beam (PVB) was proposed which exhibits a constant annular intensity profile and a diameter that is independent of topological charge<sup>11</sup>. So far, various strategies to generate PVBs have been demonstrated such as by using an axicon lens<sup>12</sup>, a spatial light modulator (SLM)<sup>13</sup>, interferometer<sup>14</sup>, or a digital micro-mirror device (DMD)<sup>15</sup>. However, all of these conventional methods to generate PVBs require a series of bulky photonic components with large footprints that have to be well aligned with respect to each other, and a physical free-space distance between them that cannot be simply downsized – hindering miniaturization and reduction of complexity of such multi-element photonic systems into something that is easily manufacturable, compact and alignment-free. Furthermore, any misalignment or incompatibility between individual optical elements results in undesired aberrations that deteriorate the quality of the generated PVBs.

Metasurfaces, which are planar optical elements composed of subwavelength artificial meta-atoms, have been proposed as a potential candidate for manipulating light in a compact footprint<sup>16-18</sup>. Their ability to arbitrarily manipulate phase, polarization, and amplitude of incident electromagnetic waves at a subwavelength scale, has opened up new opportunities for implementing multiple optical functions into a single layer optic such as meta-holograms<sup>19-21</sup>, high-resolution imaging<sup>22-24</sup>, structural color<sup>25,26</sup>, and multi-dimensional light-fields manipulation<sup>27-33</sup>. Recently, researchers have also demonstrated an approach of using a plasmonic metasurface to generate PVBs<sup>34</sup>. However, due to the dissipative losses caused by

metallic nanostructures in a plasmonic metasurface, the efficiency in the visible region is severely restricted. Another approach, leveraging a Si metasurface to generate PVBs relies on a design that requires simultaneous phase and amplitude modulation, thereby limiting the generation efficiency and operation bandwidth<sup>35</sup>.

In this work, we demonstrate the efficient and broadband generation of PVBs at visible wavelengths using a single layer dielectric metasurface. The metasurface is composed of identical rectangular cross-section TiO<sub>2</sub> nanopillars, acting as nanoscale half-waveplates, with spatially varying in-plane rotation angles, and able to impart the desired geometric phase profile on the incident light. In experiments, the generated vortex beams carrying OAM with different topological charges exhibit the same radial intensity profiles, which confirms their “perfect” characteristics. Furthermore, by adjusting the geometrical parameters of the metasurface, we show that a PVB with an arbitrary combination of topological charge, ellipticity, and size can be generated, which increases the degree of freedom in their design. Our work provides a potential approach for the development of an ultracompact nanophotonic platform for the generation of structured light beams.

## 2. Results and Discussions

### 2.1 Design of geometric metasurface to generate PVB

In theory, a PVB, whose size of radial intensity profile is independent of the topological charge, can be generated by performing Fourier transform of a Bessel beam<sup>36</sup>. However, it is difficult to generate ideal Bessel beams in practice due to their infinite energy. As an alternative approach, PVBs can also be generated by using a higher-order Bessel-Gaussian beam, which typically relies on an optical setup that includes a spiral phase plate, an axicon lens and a Fourier transform lens<sup>37</sup> (Fig. 1a). First, the spiral phase plate adds a radial phase variation from 0 to multiple of  $2\pi$  to an incident Gaussian beam and transforms it into a Laguerre-Gaussian beam. Next, an axicon lens is used to obtain the corresponding Bessel-Gaussian beam. The transverse electric field distribution of the modified Bessel-Gaussian beam can be written in Cartesian coordinates  $(x, y)$  as:

$$E_{BG}(x, y) = J_l(k_r \sqrt{x^2/a^2 + y^2/b^2}) \exp [il \arctan (\frac{ay}{bx})] \quad (1)$$

where  $l$  is the topological charge,  $a$  and  $b$  respectively are the horizontal and vertical normalizing factor,  $J_l$  is the  $l$ -th modified order Bessel function of the first kind,  $k_r$  is the radial wavenumber relating to the numerical aperture ( $NA$ ) of the axicon. Finally, a refractive lens is implemented to perform the Fourier transform of the higher-order Bessel-Gaussian beam and generate a PVB. The PVB is recorded in the rear focal plane of the refractive lens, and its transverse electric field distribution can be written in polar coordinates  $(r, \theta)$  as:

$$E_{PV}(r, \theta) = i^{l-1} \frac{\omega_g}{\omega_b} \exp(il\theta) \exp\left(\frac{-(r-R)^2}{\omega_\varepsilon^2}\right) \quad (2)$$

where  $\omega_g$  is the waist of the input Gaussian beam,  $\omega_\varepsilon$  is the waist of the Gaussian beam in the rear focal plane,  $R = \varepsilon k_r f / k$  is the radius of the PVB,  $\varepsilon = a/b$  determines the ellipticity of PVB,  $k_r$  is the radial wavevector,  $k$  is the wavevector in free-space and  $f$  is the focal length of the Fourier transform lens. The size of the generated PVB along the vertical and horizontal directions can be respectively calculated as  $R_v = afNA$  and  $R_h = bfNA$ . Given the fixed values of three parameters  $(\varepsilon, f, NA)$ , the shape of PVB can be determined and is independent of the topological charge.

In order to generate PVBs, we consider that the designed metasurface has to possess the total phase profiles of a spiral phase plate, an axicon and a Fourier transform lens, *i.e.*,  $\varphi_{meta}(x, y) = \varphi_{spiral}(x, y) + \varphi_{axicon}(x, y) + \varphi_{lens}(x, y)$  (Fig.1b). The phase distribution of the spiral phase plate can be expressed as:

$$\varphi_{spiral}(x, y) = l \cdot \arctan\left(\frac{ay}{bx}\right) \quad (3)$$

The phase imparted to the incident light from an axicon can be expressed as:

$$\varphi_{axicon}(x, y) = -\frac{2\pi}{\lambda} \sqrt{x^2/a^2 + y^2/b^2} \cdot NA \quad (4)$$

where  $\lambda$  is the operating wavelength. Lastly, the phase of the Fourier transform lens takes the form:

$$\varphi_{lens}(x, y) = -\frac{\pi}{\lambda f} (x^2 + y^2) \quad (5)$$

Fig. 1c shows the schematic diagram of the proposed planar metasurface, where it is evident that when compared to the conventional bulk-optic combinations, the metasurface PVB generator significantly simplifies the optical setup. The basic unit-cell of the metasurface is a rectangular  $\text{TiO}_2$  nanopillar of height,  $H = 600$  nm, arranged spatially on a fused-silica substrate

with a nominal lattice constant,  $P = 350$  nm (Fig. 1d). The choice of material,  $\text{TiO}_2$ , is governed both by its high refractive index and low-loss at visible frequencies as well as by our capabilities to deposit and pattern thin-films of  $\text{TiO}_2$  into high aspect-ratio nanostructures. For an incident circularly polarized light, Pancharatnam-Berry (PB) or geometric phase, is obtained by rotating anisotropic rectangular nanopillars acting as half-waveplates to yield a local phase shift given by  $\varphi_{PB}(x, y) = 2\theta(x, y)$ , where  $\theta$  is the in-plane orientation angle of the nanopillar with respect to the fast axis. For PVB generation, the required PB phase  $\varphi_{PB}(x, y)$  must be equal to  $\varphi_{PV}(x, y)$ , hence the rotation angle  $\theta(x, y)$  of each nanopillar spatially can be simply determined to be  $\theta(x, y) = \varphi_{PV}(x, y)/2$ .

A geometric-phase-based metasurface converts an incident circularly polarized beam into a cross-polarized beam with opposite helicity and adds an additional phase shift. Therefore, to improve the generation efficiency of PVBs using such a metasurface, optimization of the polarization conversion efficiency (PCE) of the metasurface unit-cell is a primary prerequisite. At a central visible wavelength of 530 nm, the structural parameters of the nanopillars are optimized by using finite-difference time-domain (FDTD) simulations, and the corresponding complex transmission coefficients are given in Supplementary Fig. S1. The transmittance for circularly polarized light is calculated as  $|t_{cross}|^2 = \frac{1}{4}(\sqrt{|t_x|^2}e^{i\varphi_x} - \sqrt{|t_y|^2}e^{i\varphi_y})^2$  and  $|t_{co}|^2 = \frac{1}{4}(\sqrt{|t_x|^2}e^{i\varphi_x} + \sqrt{|t_y|^2}e^{i\varphi_y})^2$ , where  $t_x$ ,  $t_y$ ,  $\varphi_x$ ,  $\varphi_y$  are the transmission coefficients and phase shifts for linearly polarized light along the  $x$  and  $y$  axis, respectively. The polarization conversion efficiency defined as,  $\text{PCE} = \frac{|t_{cross}|^2}{|t_{co}|^2 + |t_{cross}|^2} = \frac{T_{cross}}{T_{co} + T_{cross}}$ , calculated at a wavelength of 530 nm is shown in Fig. 1e. To obtain a high PCE, the width and length of the nanopillar are chosen to be  $W = 100$  nm and  $L = 250$  nm (black dot, Fig. 1e). For this nanopillar dimension, the average PCE calculated from the values of  $t_{cross}$  and  $t_{co}$  (Fig. 1f) was determined to also be relatively high across the entire visible range. In addition, the nanopillar also exhibits phase retardation close to  $\pi$  between the  $x$ - and  $y$ -polarization components (Fig. 1g), which is a prerequisite for good half-waveplate operation across a broad wavelength range. These two features guarantee an efficient broadband response of the metasurface for visible light. Figure 1h shows the optical microscope image of the

fabricated metasurface PVB generator, and the inset shows a scanning electron microscope (SEM) image of the constituent nanopillars. The detailed fabrication process of the metasurface, based on damascene lithography, is described in the experimental section. The fabricated metasurface has an overall nominal size of  $90\ \mu\text{m} \times 90\ \mu\text{m}$  with a designed focal length  $f = 150\ \mu\text{m}$  at a wavelength of 530 nm. Figure 1i shows the schematic diagram of the setup for the optical characterization of the metasurface PVB generator. A supercontinuum laser attached to an acousto-optic tunable filter (AOTF) is used to generate a collimated, linearly polarized laser beam at any desired wavelength in the visible spectral range. The incident light is then converted into a circularly polarized beam using a combination of a linear polarizer and an achromatic quarter-wave plate (QWP) before illuminating the metasurface at normal incidence. The transmitted light containing cross-polarized and co-polarized components through the metasurface is collected using an objective with  $20\times$  magnification. Another pair of QWP and a linear polarizer is then used to block any background undesired, zero-order, co-polarized components directly transmitted through the metasurface, and finally, the entire light field distribution is captured using a charge-coupled device (CCD) camera.

## 2.2 Broadband generation of PVBs for visible light

Figure 2a shows the experimentally measured intensity distributions of the vortex beams generated by the metasurface with topological charges ranging from  $l = 1$  to  $l = 4$  at free-space wavelengths of 450 nm, 530 nm, and 630 nm, respectively. Except for the variation in topological charge, the four metasurfaces characterized here have the same design parameters of  $NA = 0.08$  and  $\varepsilon = 1$  (see corresponding optical microscope images in Supplementary Fig. S2). The topological charge of the generated vortex beam can be easily identified by examining the number of spiral branches in the measured interference patterns (Fig. 2b), which are created by interfering the generated vortex beam with a co-propagating Gaussian beam. It can be clearly seen that the number of branches in the interference images from top to bottom is 1, 2, 3 and 4, respectively, corresponding to topological charge varying from  $l = 1$  to  $l = 4$ . Although the metasurface exhibits a broadband response for visible light, due to the existence of material dispersion, the focal distances at different wavelengths vary correspondingly. For example, at nominal propagation distances away from the metasurface exit surface,  $z = 180\ \mu\text{m}$  and  $128\ \mu\text{m}$

corresponding to focal positions for blue (450 nm) and red (630 nm) light, respectively, the in-plane annular intensity patterns are identical to the ones for green light (530 nm) at a designed focal position of  $z = 150 \mu\text{m}$ . Figure 2c-f shows the cross-sections of the normalized intensity profiles extracted along the  $y$ -direction at the wavelength of 530 nm. The consistent cross-sectional intensity profiles verify that the sizes of the generated vortex beams are insensitive to the topological charges. The measured diameters of the generated vortex beams with  $l = 1$  to  $l = 4$  are  $(23.25 \pm 0.12) \mu\text{m}$ ,  $(24.28 \pm 0.09) \mu\text{m}$ ,  $(24.04 \pm 0.12) \mu\text{m}$  and  $(24.28 \pm 0.08) \mu\text{m}$ , respectively, which agree well with the theoretically calculated value of  $24 \mu\text{m}$ . The measured diameters were determined by fitting a Gaussian curve to the experimental results, and the uncertainty is one standard deviation (SD) of the Gaussian fit parameter. The generation efficiencies of the metasurfaces (the intensity of generated PVBs divided by the total incident intensity) are  $(27 \pm 2) \%$  at 450 nm,  $(68 \pm 3) \%$  at 530 nm and  $(46 \pm 2) \%$  at 630 nm, which can be further improved by optimizing the fabrication process to achieve smooth sidewalls, and rectangular cross-section nanopillars with no sidewall tapering. The uncertainty in efficiency measurements are one SD for repeated measurements. Further experimental results of the measured  $y$ - $z$  plane intensity distributions and their cross-sections at different wavelengths are given in Supplementary Fig. S3 and S4.

### 2.3 Generation of elliptical and size-controllable PVBs

In addition to standard circular PVBs, through modification in the design parameters, the metasurface can also be used to generate arbitrary elliptical PVBs. Here we design eight metasurfaces with two ellipticities  $\varepsilon = 0.8$  and  $\varepsilon = 1.2$  (see corresponding optical microscope images in Supplementary Fig. S5). Figure 3a shows the experimentally captured intensity distributions of elliptical vortex beams with topological charge varying from  $l = 1$  to  $l = 4$  at free space wavelengths of 450 nm, 530 nm and 630 nm. The corresponding interference patterns recorded to confirm their topological charges are shown in Supplementary Fig. S6. Similar to the circular case shown in Fig. 2, the sizes of the intensity distribution of elliptical vortex beams with different topological charges are identical, which verifies their perfect characteristics. Figure 3b-i show the cross-sections of the normalized intensity of vortex beams at the wavelength of 530 nm. For  $\varepsilon = 0.8$ , horizontal/vertical diameters are measured as  $(23.51 \pm$

$0.11) \mu\text{m} / (18.42 \pm 0.07) \mu\text{m}$ ,  $(23.63 \pm 0.07) \mu\text{m} / (18.78 \pm 0.09) \mu\text{m}$ ,  $(23.87 \pm 0.12) \mu\text{m} / (18.78 \pm 0.15) \mu\text{m}$ ,  $(23.87 \pm 0.05) \mu\text{m} / (18.90 \pm 0.08) \mu\text{m}$ , respectively for  $l = 1$  to 4 (Fig. 3b-e). For  $\varepsilon = 1.2$ , the horizontal/vertical diameter are measured as  $(23.15 \pm 0.09) \mu\text{m} / (28.12 \pm 0.12) \mu\text{m}$ ,  $(23.27 \pm 0.11) \mu\text{m} / (28.00 \pm 0.07) \mu\text{m}$ ,  $(23.87 \pm 0.12) \mu\text{m} / (28.12 \pm 0.12) \mu\text{m}$ ,  $(23.63 \pm 0.12) \mu\text{m} / (28.42 \pm 0.11) \mu\text{m}$ , respectively for  $l = 1$  to 4 (Fig. 3f-i). The uncertainties in diameter measurements are one SD of the Gaussian fit parameter. These values agree well with the theoretical horizontal/vertical diameter  $24 \mu\text{m} / 19.2 \mu\text{m}$  for  $\varepsilon = 0.8$  and  $24 \mu\text{m} / 28.8 \mu\text{m}$  for  $\varepsilon = 1.2$ . Further experimental results of the measured  $y$ - $z$  plane intensity distributions and their cross-sections at different wavelengths are given in supplementary Fig. S7 and S8.

Finally, besides independent manipulation of topological charge and ellipticity of the vortex beams, the metasurface can also be used to arbitrarily control the size of generated PVB by adjusting the numerical aperture ( $NA$ ). Figure 4a shows the measured normalized intensity distributions of the PVBs ( $\varepsilon = 0.8$ ,  $\varepsilon = 1$ ,  $\varepsilon = 1.2$ ) with topological charges of  $l = 1$  and  $l = 4$  which are generated by metasurfaces designed with different numerical apertures ( $NA = 0.1$  and  $NA = 0.15$ ) (see corresponding optical microscope images in Supplementary Fig. S9). The measured  $y$ - $z$  plane intensity distributions and their corresponding interference patterns to confirm the topological charges are shown in Supplementary Fig. S10 and S11, respectively. It can be clearly seen that, although the vortex beams are insensitive to the topological charge, their sizes are proportional to the numerical aperture of the metasurface. Figure 4b-g show the vertical cross-sections of the normalized intensity of vortex beams at the  $x$ - $y$  plane at a wavelength of 530 nm. The measured horizontal/vertical diameters of PVBs for  $NA = 0.1$  and 0.15 are summarized in Supplementary Table S1, which agree well with the theoretically calculated values. Further experimental results of cross-sections at different wavelengths are given in Supplementary Fig. S12. These results clearly show that not only the generated vortex beam has “perfect” characteristics, its shape and size can also be independently controlled, which further enriches the design freedom of vortex beams generated using metasurfaces.

### 3. Conclusions

The use of ultra-compact, multifunctional photonic elements to efficiently generate structured

light fields is of far-reaching significance for photonics research. Undoubtedly, as a promising platform, complimentary to the developments in integrated photonics, metasurfaces are serving as a crucial component for photonic device research. In this work, we exploit an ultrathin dielectric metasurface composed of TiO<sub>2</sub> nanopillars to efficiently generate perfect vortex beams in the visible spectral range. Through optimization of the nanopillars' structural parameters, the experimentally generated vortex beams carrying OAM with different topological charges exhibit the same radial intensity profiles, verifying their perfect characteristics. In addition, by varying their ellipticity factor and numerical aperture, the shape and size of the generated perfect vortex beams can be independently manipulated. We envision that this work will inspire the creation of flat nanophotonic platforms for efficient generation and control of structured light beams and further promote their practical applications in areas such as optical communication, optical data storage, and quantum information science.

## **4. Experimental Section**

### **Numerical optimization**

Finite-difference time-domain (FDTD) simulations are performed for optimization of the basic unit-cell structure with an area of 350 nm × 350 nm in the  $x$ - $y$  plane using periodic boundary conditions. Perfectly matched layers (PML) conditions are employed along the  $z$ -direction. The  $x$ - and  $y$ -polarization plane waves were normally incident on the unit cell along the  $z$ -direction.

### **Metasurface Fabrication**

A layer of hexamethyldisilazane (HMDS) was prime-vapor-coated on a 500 μm thick fused silica substrate and then spin-coated with a layer of 600 nm thick, high-resolution, positive-tone electron-beam resist. The thickness of 600 nm determines the height of the nanopillars. Next, the sample was coated with a layer of 10 nm thick aluminum by thermal evaporation to avoid the charging effect generated in the following electron-beam lithography step. The accelerating voltage and beam current of the e-beam lithography were set at 100 kV and 2 nA, respectively. Resist development was done in hexyl-acetate for 120 s. The patterned sample was coated with TiO<sub>2</sub> using an atomic layer deposition (ALD) system at a temperature of 90 °C. After the ALD step, etching was performed using an inductively coupled plasma reactive ion

etching (ICP-RIE), with a gas mixture of  $\text{Cl}_2$  and  $\text{BCl}_3$ . The etching was stopped when the electron-beam resist was exposed. Finally, the sample was exposed to ultraviolet irradiation, followed by soaking in n-methyl-2-pyrrolidone, which removes the resist and produce the metasurface with predesigned geometrical parameters.

## Reference

1. L. Allen, M. W. Beijersbergen, R. J. C. Spreeuw & J. P. Woerdman. Orbital Angular-Momentum of Light and the Transformation of Laguerre-Gaussian Laser Modes. *Physical Review A* 45, 8185-8189 (1992).
2. X. L. Cai, J. W. Wang, M. J. Strain, B. Johnson-Morris, J. B. Zhu, M. Sorel, J. L. O'Brien, M. G. Thompson & S. Y. Yu. Integrated Compact Optical Vortex Beam Emitters. *Science* 338, 363-366 (2012).
3. A. Mair, A. Vaziri, G. Weihs & A. Zeilinger. Entanglement of the orbital angular momentum states of photons. *Nature* 412, 313-316 (2001).
4. G. Molina-Terriza, J. P. Torres & L. Torner. Twisted photons. *Nature Physics* 3, 305-310 (2007).
5. K. T. Gahagan & G. A. Swartzlander. Optical vortex trapping of particles. *Optics Letters* 21, 827-829 (1996).
6. M. Dienerowitz, M. Mazilu, P. J. Reece, T. F. Krauss & K. Dholakia. Optical vortex trap for resonant confinement of metal nanoparticles. *Optics Express* 16, 4991-4999 (2008).
7. J. H. Kang, K. Kim, H. S. Ee, Y. H. Lee, T. Y. Yoon, M. K. Seo & H. G. Park. Low-power nano-optical vortex trapping via plasmonic diablo nanoantennas. *Nature Communications* 2, 582 (2011).
8. D. G. Grier. A revolution in optical manipulation. *Nature* 424, 810-816 (2003).
9. Y. J. Shen, X. J. Wang, Z. W. Xie, C. J. Min, X. Fu, Q. Liu, M. L. Gong & X. C. Yuan. Optical vortices 30 years on: OAM manipulation from topological charge to multiple singularities. *Light-Science & Applications* 890 (2019).
10. H. W. Yan, E. T. Zhang, B. Y. Zhao & K. L. Duan. Free-space propagation of guided optical vortices excited in an annular core fiber. *Optics Express* 20, 17904-17915 (2012).
11. A. S. Ostrovsky, C. Rickenstorff-Parrao & V. Arrizón. Generation of the "perfect" optical

- vortex using a liquid-crystal spatial light modulator. *Optics Letters* 38, 534-536 (2013).
12. M. V. Jabir, N. A. Chaitanya, A. Aadhi & G. K. Samanta. Generation of "perfect" vortex of variable size and its effect in angular spectrum of the down-converted photons. *Scientific Reports* 6, 21877 (2016).
  13. P. Vaity & L. Rusch. Perfect vortex beam: Fourier transformation of a Bessel beam. *Optics Letters* 40, 597-600 (2015).
  14. T. L. Wang, S. Y. Fu, F. He & C. Q. Gao. Generation of perfect polarization vortices using combined gratings in a single spatial light modulator. *Applied Optics* 56, 7567-7571 (2017).
  15. C. L. Zhang, C. J. Min & X. C. Yuan. Shaping perfect optical vortex with amplitude modulated using a digital micro-mirror device. *Optics Communications* 381, 292-295 (2016).
  16. A. V. Kildishev, A. Boltasseva & V. M. Shalaev. Planar Photonics with Metasurfaces. *Science* 339, 1232009 (2013).
  17. D. M. Lin, P. Y. Fan, E. Hasman & M. L. Brongersma. Dielectric gradient metasurface optical elements. *Science* 345, 298-302 (2014).
  18. N. F. Yu & F. Capasso. Flat optics with designer metasurfaces. *Nature Materials* 13, 139-150 (2014).
  19. X. J. Ni, A. V. Kildishev & V. M. Shalaev. Metasurface holograms for visible light. *Nature Communications* 4, 2807 (2013).
  20. G. X. Zheng, H. Muhlenbernd, M. Kenney, G. X. Li, T. Zentgraf & S. Zhang. Metasurface holograms reaching 80% efficiency. *Nature Nanotechnology* 10, 308-312 (2015).
  21. G. Y. Qu, W. H. Yang, Q. H. Song, Y. L. Liu, C. W. Qiu, J. C. Han, D. P. Tsai & S. M. Xiao. Reprogrammable meta-hologram for optical encryption. *Nature Communications* 11, 5484 (2020).
  22. M. Khorasaninejad, W. T. Chen, R. C. Devlin, J. Oh, A. Y. Zhu & F. Capasso. Metalenses at visible wavelengths: Diffraction-limited focusing and subwavelength resolution imaging. *Science* 352, 1190-1194 (2016).
  23. R. J. Lin, V. C. Su, S. M. Wang, M. K. Chen, T. L. Chung, Y. H. Chen, H. Y. Kuo, J. W. Chen, J. Chen, Y. T. Huang, J. H. Wang, C. H. Chu, P. C. Wu, T. Li, Z. L. Wang, S. N. Zhu & D. P. Tsai. Achromatic metalens array for full-colour light-field imaging. *Nature Nanotechnology* 14, 227-231 (2019).

24. C. Schlickriede, S. S. Kruk, L. Wang, B. Sain, Y. Kivshar & T. Zentgraf. Nonlinear Imaging with All-Dielectric Metasurfaces. *Nano Letters* 20, 4370-4376 (2020).
25. W. H. Yang, S. M. Xiao, Q. H. Song, Y. L. Liu, Y. K. Wu, S. Wang, J. Yu, J. C. Han & D. P. Tsai. All-dielectric metasurface for high-performance structural color. *Nature Communications* 11, 1864 (2020).
26. P. C. Huo, M. W. Song, W. Q. Zhu, C. Zhang, L. Chen, H. J. Lezec, Y. Q. Lu, A. Agrawal & T. Xu. Photorealistic full-color nanopainting enabled by a low-loss metasurface. *Optica* 7, 1171-1172 (2020).
27. A. Arbabi, Y. Horie, M. Bagheri & A. Faraon. Dielectric metasurfaces for complete control of phase and polarization with subwavelength spatial resolution and high transmission. *Nature Nanotechnology* 10, 937- 943 (2015).
28. S. Q. Chen, W. W. Liu, Z. C. Li, H. Cheng & J. G. Tian. Metasurface-Empowered Optical Multiplexing and Multifunction. *Advanced Materials* 32,1805912 (2020).
29. H. Sroor, Y. W. Huang, B. Sephton, D. Naidoo, A. Valles, V. Ginis, C. W. Qiu, A. Ambrosio, F. Capasso & A. Forbes. High-purity orbital angular momentum states from a visible metasurface laser. *Nature Photonics* 14, 498-503 (2020).
30. Z. P. Li, X. Tian, C. W. Qiu & J. S. Ho. Metasurfaces for bioelectronics and healthcare. *Nature Electronics* 4, 382–391 (2021).
31. X. Xie, M. B. Pu, J. J. Jin, M. F. Xu, Y. H. Guo, X. Li, P. Gao, X. L. Ma & X. G. Luo. Generalized Pancharatnam-Berry Phase in Rotationally Symmetric Meta-Atoms. *Physical Review Letters* 126, 183902 (2021).
32. M. Z. Liu, W. Q. Zhu, P. C. Huo, L. Feng, M. W. Song, C. Zhang, L. Chen, H. J. Lezec, Y. Q. Lu, A. Agrawal & T. Xu. Multifunctional metasurfaces enabled by simultaneous and independent control of phase and amplitude for orthogonal polarization states. *Light-Science & Applications* 10, 107 (2021)
33. M. Z. Liu, P. C. Huo, W. Q. Zhu, C. Zhang, S. Zhang, M. W. Song, S. Zhang, Q. W. Zhou, L. Chen, H. J. Lezec, A. Agrawal, Y. Q. Lu & T. Xu. Broadband generation of perfect Poincare beams via dielectric spin-multiplexed metasurface. *Nature Communications* 12, 2230 (2021).
34. Y. C. Zhang, W. W. Liu, J. Gao & X. D. Yang. Generating Focused 3D Perfect Vortex Beams By Plasmonic Metasurfaces. *Advanced Optical Materials* 6, 1701228 (2018).

35. Y. J. Bao, J. C. Ni & C. W. Qiu. A Minimalist Single-Layer Metasurface for Arbitrary and Full Control of Vector Vortex Beams. *Advanced Materials* 32, 1905659 (2020).
36. D. L. Li, C. L. Chang, S. P. Nie, S. T. Feng, J. Ma & C. J. Yuan. Generation of elliptic perfect optical vortex and elliptic perfect vector beam by modulating the dynamic and geometric phase. *Applied Physics Letters* 113, 121101 (2018).
37. Y. C. Liu, Y. G. Ke, J. X. Zhou, Y. Y. Liu, H. L. Luo, S. C. Wen & D. Y. Fan. Generation of perfect vortex and vector beams based on Pancharatnam-Berry phase elements. *Scientific Reports* 7 (2017).

### **Acknowledgements**

The work is partially supported by the Key Research and Development Program from Ministry of Science and Technology of China under Grant No. 2017YFA0303700. W. Z., L. C. and A. A. acknowledge support under the Cooperative Research Agreement between the University of Maryland and the National Institute of Standards and Technology Physical Measurement Laboratory, Award #70NANB14H209. Q. Z., M. L. and W. Z. contributed equally to this work.

### **Notes**

The authors declare no competing interests.

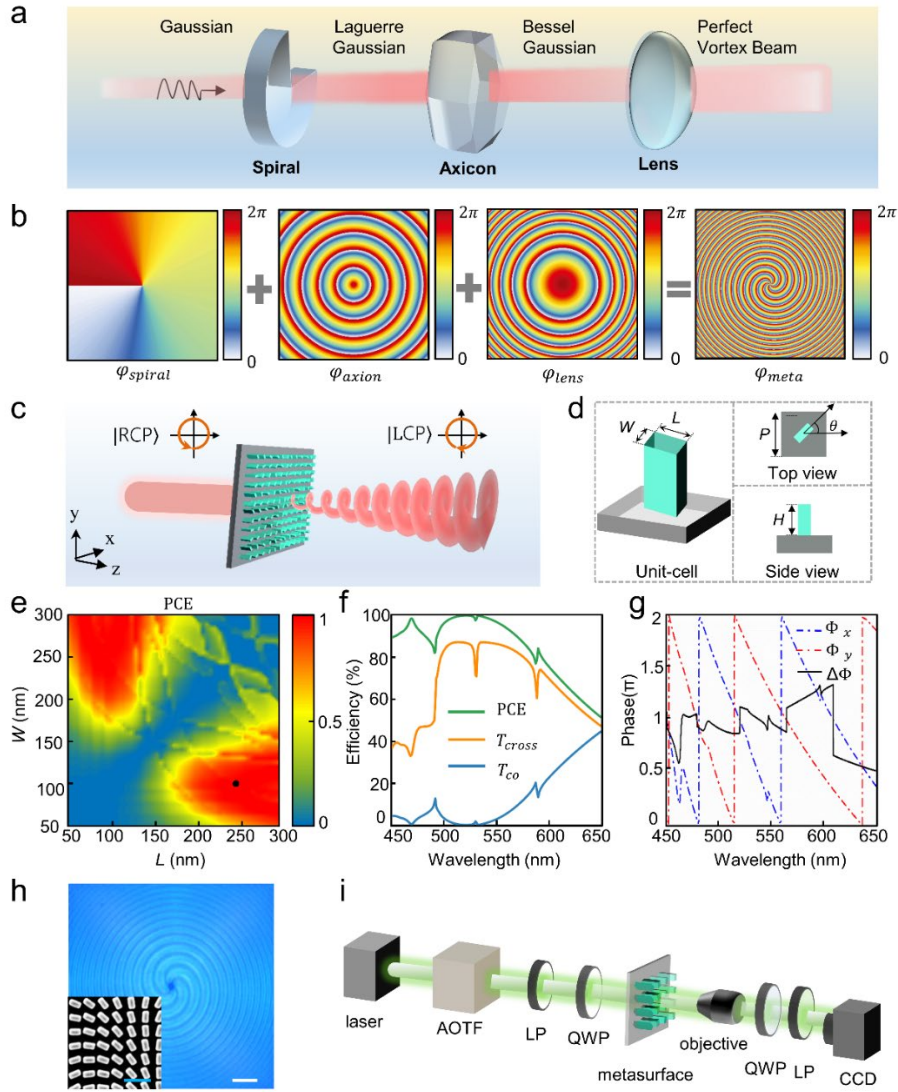


Figure 1. a. Schematic of the PVBs generation process using traditional bulk optical elements. b. The phase profile of the designed metasurface which superimposes three-phase profiles of a spiral, an axicon, and a lens. c. Schematic illustration of the designed metasurface with nanopillar arrays generating PVBs for right-circularly polarized (RCP) light. For the RCP beam, part of the light changes handedness to left-circularly polarized (LCP) upon propagation through the metasurface. d. Left: schematic of the unit-cell of the metasurface. Right: the top view and side view of the unit cell. e. Calculated polarization conversion efficiency as a function of nanopillars' length and width at a wavelength of 530 nm. The black dot denotes selected structural parameters of the nanopillar. f. Distribution of transmittance of cross-polarization and co-polarization components as a function of wavelength ranging from 450 nm to 650 nm. g. Calculated phase  $\phi_x$ ,  $\phi_y$  for x- and y- polarization light and their difference  $\Delta\phi$ . h. Optical microscope image of the fabricated metasurface. Scale bar: 10  $\mu\text{m}$ . Bottom-left inset shows the SEM image of the metasurface. Scale bar: 500 nm. i. Optical setup for generating and analyzing PVBs.

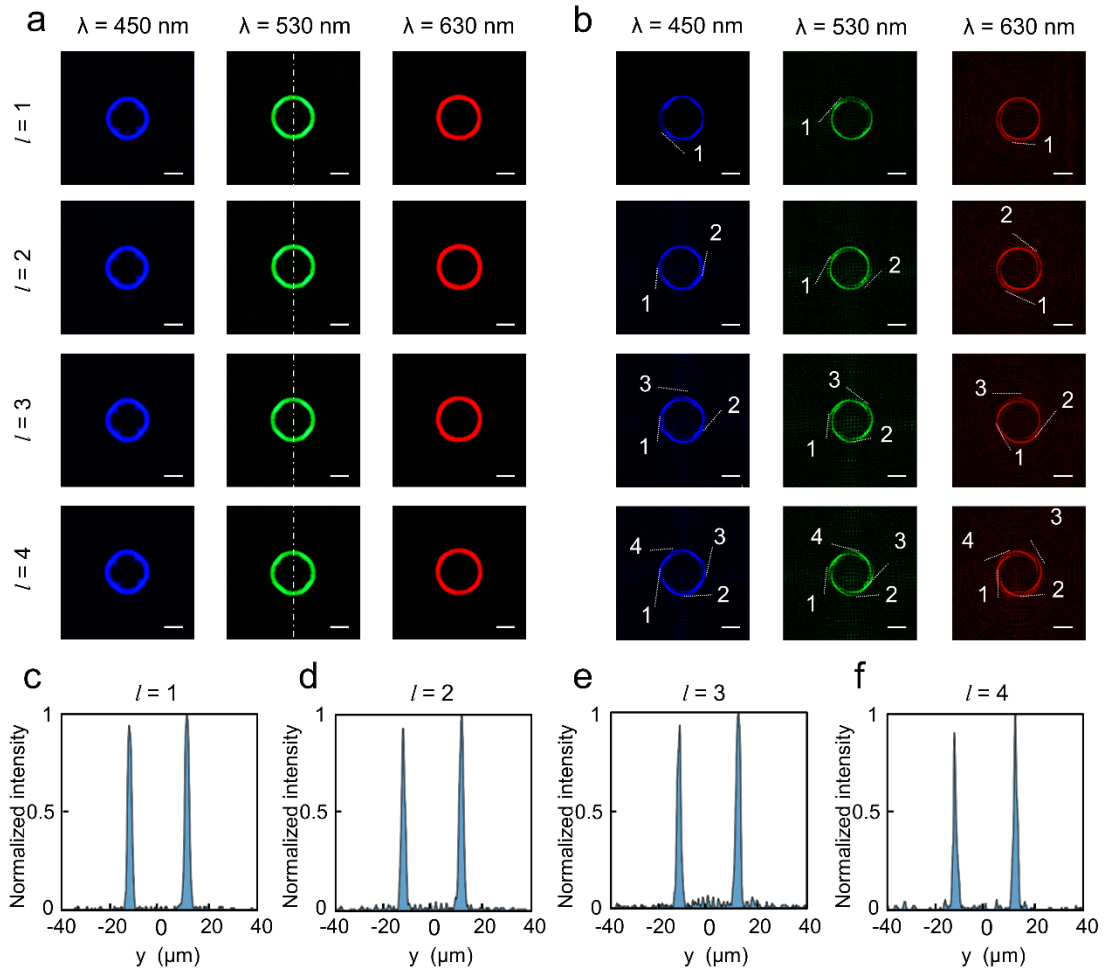


Figure 2. a. The measured annular intensity profiles of the generated PVBs ( $\varepsilon = 1$ ) with topological charges of  $l = 1, 2, 3$  and  $4$  (from top to bottom) in the  $x$ - $y$  plane at wavelengths of 450 nm (blue), 530 nm (green) and 630 nm (red) using the metasurface with  $NA = 0.08$ . The propagation distances are  $z = 180 \mu\text{m}$  (blue),  $150 \mu\text{m}$  (green) and  $128 \mu\text{m}$  (red), respectively. b. The measured interference patterns corresponding to the PVBs used to identify the number of topological charges. The dashed lines represent the tangential direction. Scale bar:  $10 \mu\text{m}$ . c-f. Normalized cross-sections of the annular intensity profiles of the PVBs along the vertical direction with topological charges  $l = 1, 2, 3, 4$  at a wavelength of 530 nm.

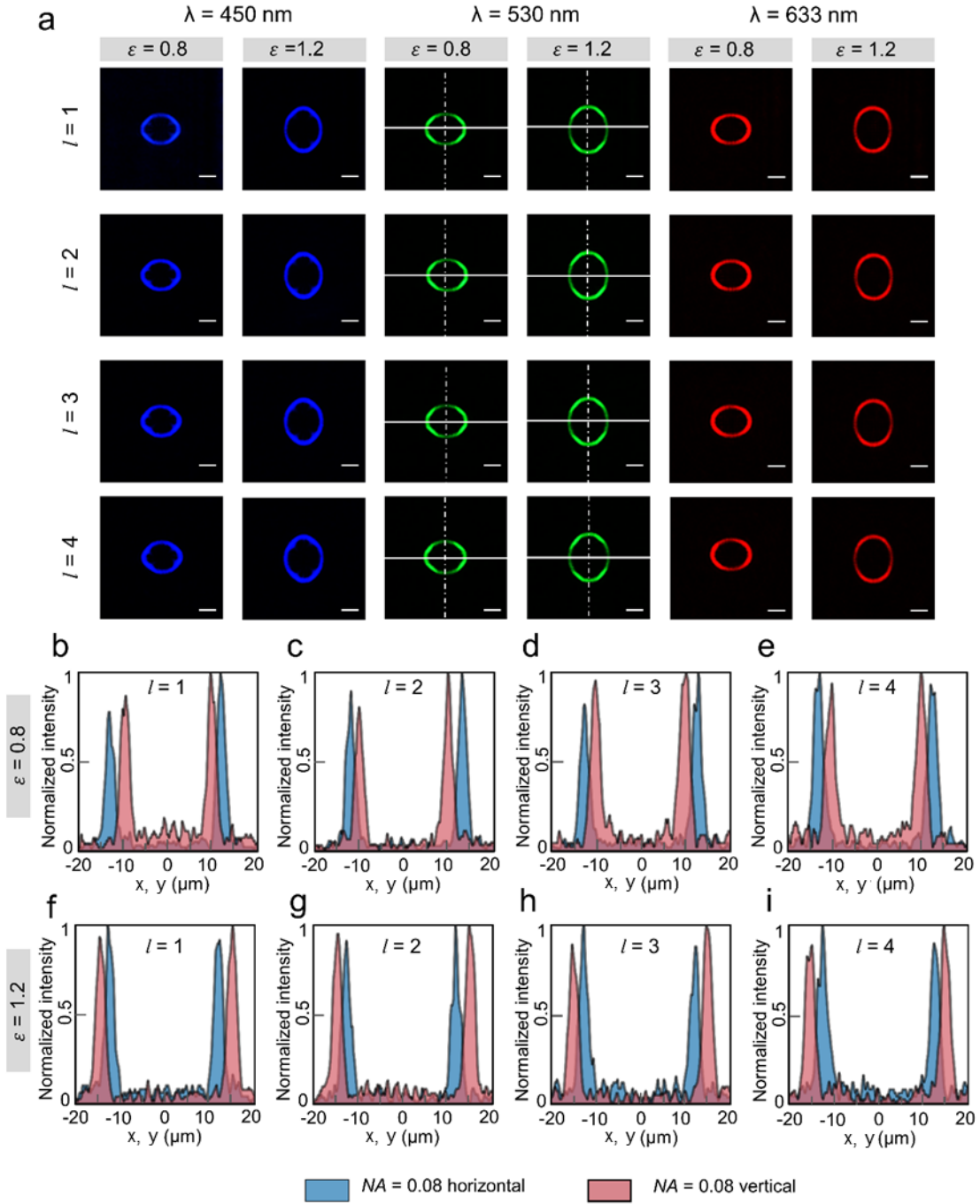


Figure 3. a. The measured annular intensity profiles of the generated PVBs ( $\epsilon = 0.8$  and  $1.2$ ) with topological charges of  $l = 1, 2, 3$  and  $4$  (from top to bottom) in the  $x$ - $y$  plane at wavelengths of  $450$  nm,  $530$  nm and  $630$  nm using the metasurface with  $NA = 0.08$ . The propagation distances are  $z = 180$   $\mu\text{m}$  (blue),  $150$   $\mu\text{m}$  (green) and  $128$  (red)  $\mu\text{m}$ , respectively. The solid line represents the horizontal direction, and the dashed line represents the vertical direction. Scale bar:  $10$   $\mu\text{m}$ . b-i. Normalized cross-sections of the annular intensity profiles of the PVBs indicated by the solid line with topological charges  $l = 1, 2, 3$ , and  $4$  at the wavelength of  $530$  nm.

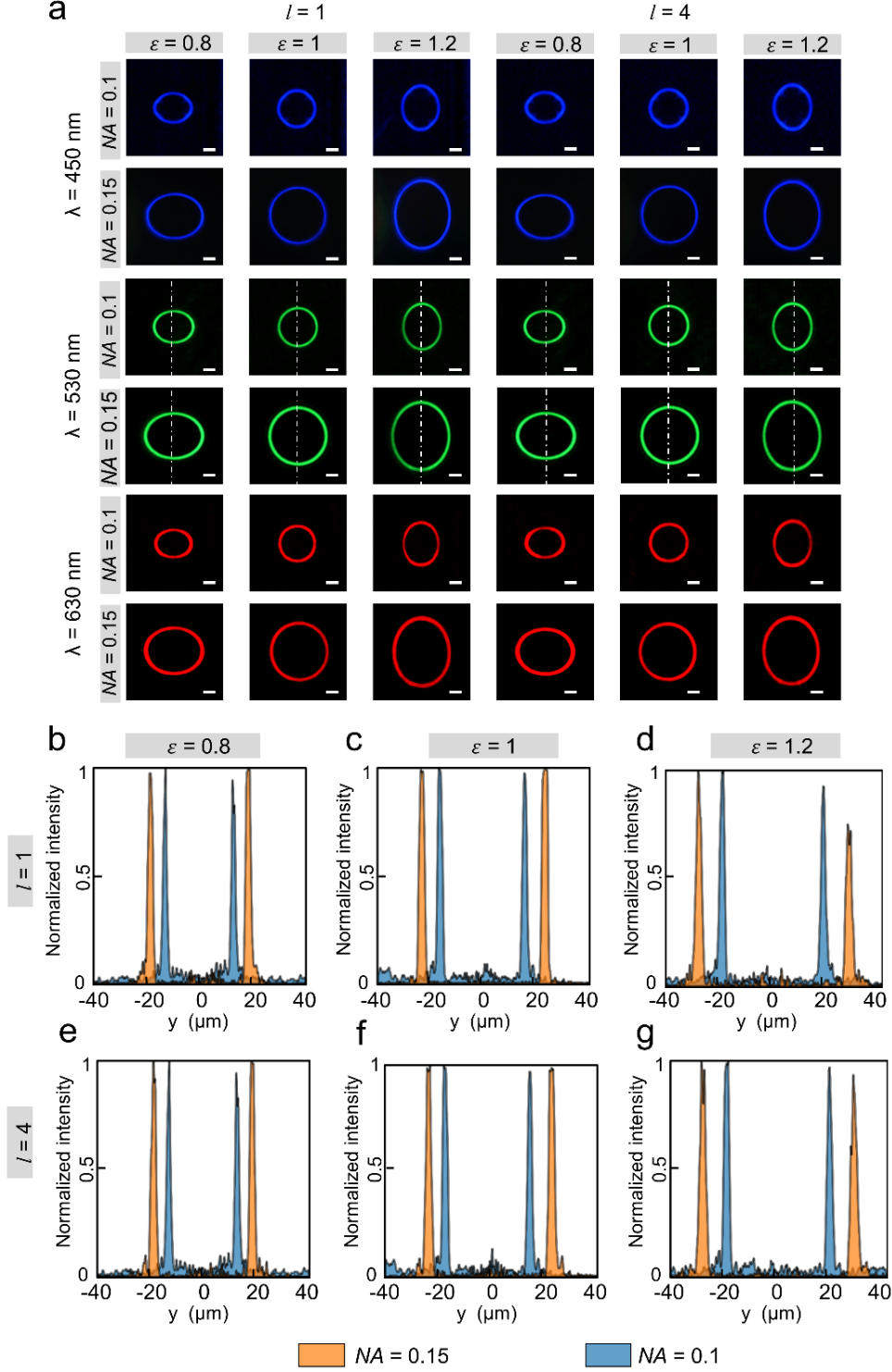


Figure 4. a. The measured annular intensity profiles of the generated PVBs ( $\epsilon = 0.8, 1$  and  $1.2$ ) with topological charges of  $l = 1$  and  $l = 4$  (from left to right) in the  $x$ - $y$  plane at wavelengths of 450 nm, 530 nm and 630 nm using two metasurfaces with  $NA = 0.1$  and  $NA = 0.15$ . The propagation distances are  $z = 180 \mu\text{m}$  (blue),  $150 \mu\text{m}$  (green) and  $128 \mu\text{m}$  (red), respectively. The dashed line represents the vertical direction. Scale bar:  $10 \mu\text{m}$ . b-g. Normalized cross-sections (along the vertical direction) of the annular intensity profiles of the PVBs with topological charges  $l = 1$  and  $l = 4$  at a wavelength of 530 nm.

## **Supplemental Material**

### **Broadband generation of perfect vortex beams by dielectric geometric metasurface for visible light**

Qianwei Zhou<sup>1,2</sup>, Mingze Liu<sup>1,2</sup>, Wenqi Zhu<sup>3,4</sup>, Lu Chen<sup>3,4</sup>, Yongze Ren<sup>1,2</sup>, Henri J. Lezec<sup>3</sup>, Yanqing Lu<sup>1,2</sup>, Amit Agrawal<sup>3,4</sup>, Ting Xu<sup>1,2</sup>

1. National Laboratory of Solid-State Microstructures, Jiangsu Key Laboratory of Artificial Functional Materials, College of Engineering and Applied Sciences, Nanjing University, Nanjing 210093, China
2. Collaborative Innovation Center of Advanced Microstructures, Nanjing 210093, China
3. Physical Measurement Laboratory, National Institute of Standards and Technology, Gaithersburg, Maryland 20899, United States
4. Maryland NanoCenter, University of Maryland, College Park, Maryland 20899, United States

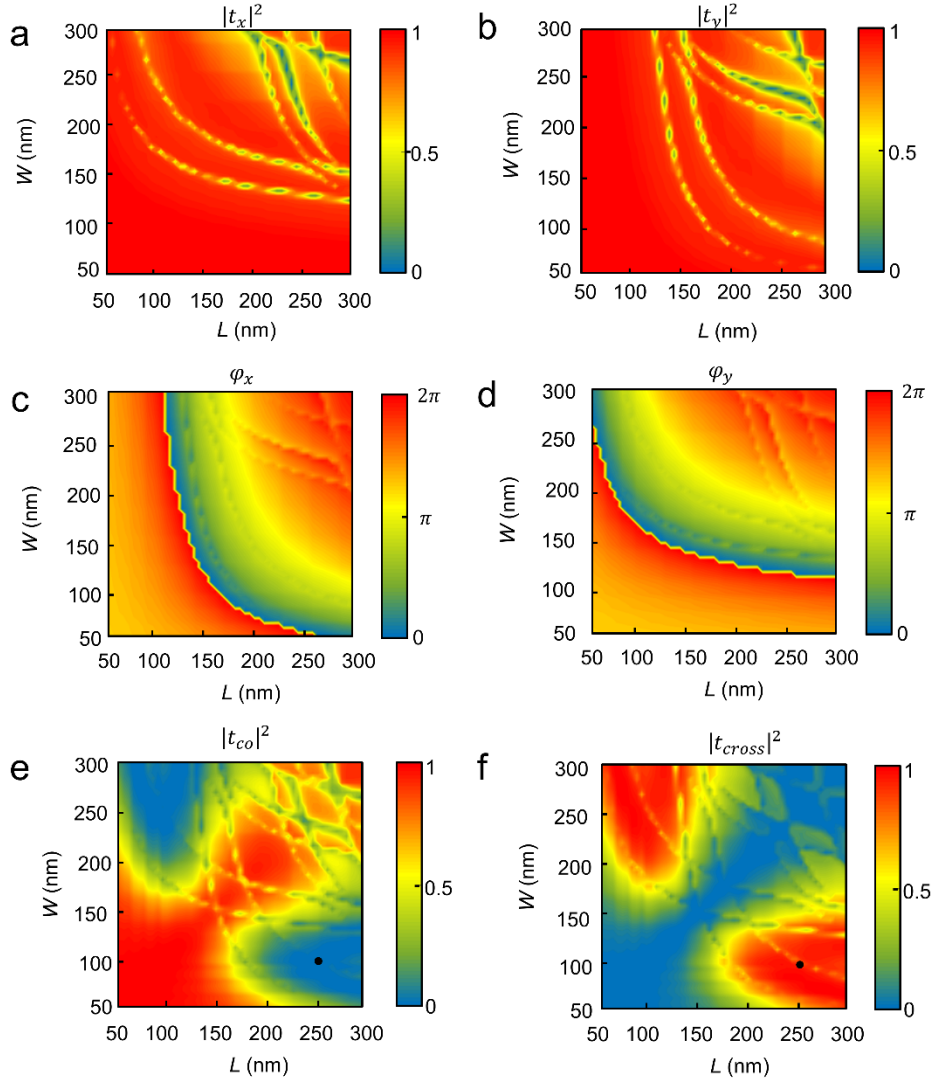


**Figure S1** Simulation data for two-dimensional parameter sweeps of  $\text{TiO}_2$  nanopillars with a height of 600 nm. (a)- (b) and (c)-(d) Simulated intensity of transmission coefficients and phase shifts of nanopillars for  $x$ - and  $y$ -polarization beam with various length  $L$  and width  $W$ . (d) and (e) Simulated intensity of each nanostructure for co-polarized and cross- polarized beams when the width  $W$  and length  $L$  are modified.

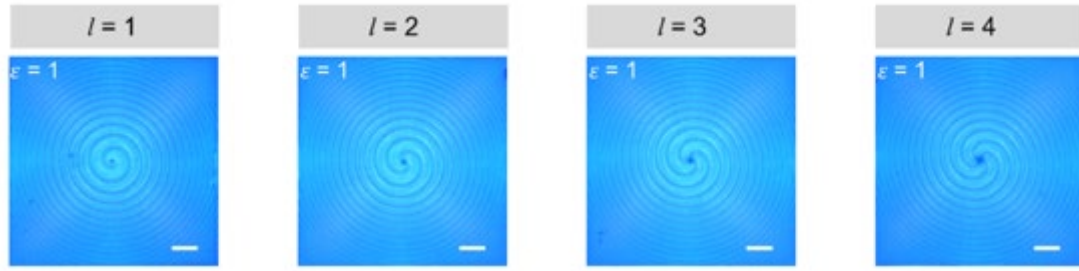


**Figure S2** Optical microscope images of the fabricated metasurfaces ( $\epsilon = 1$ ,  $NA = 0.08$ ) with topological charges of  $l = 1, 2, 3$ , and  $4$  (from left to right). Scale bar:  $10 \mu\text{m}$ .

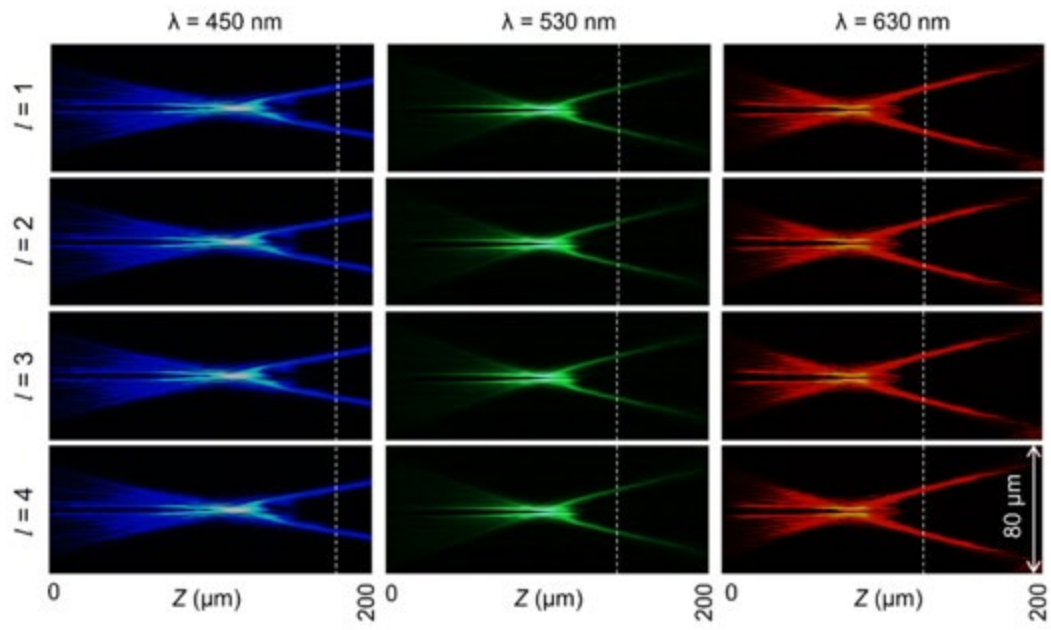


**Figure S3** The  $y$ - $z$  plane intensity distributions of the vortex beams ( $\varepsilon = 1$ ). The propagation distances represented by the white dotted line at the three wavelengths are  $z = 180 \mu\text{m}$ ,  $150 \mu\text{m}$  and  $128 \mu\text{m}$ .

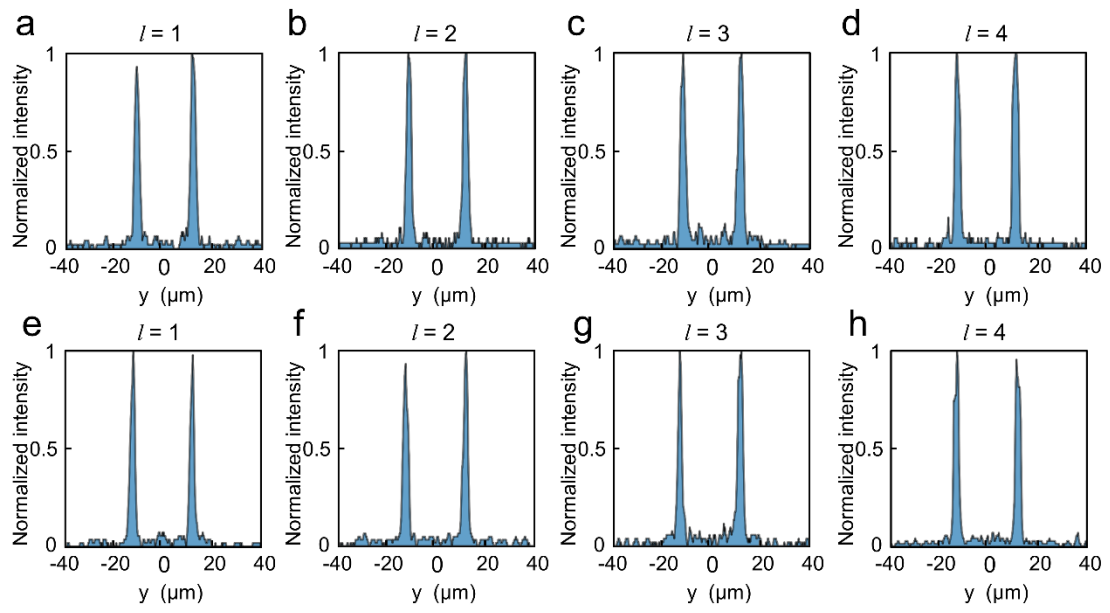


**Figure S4** Normalized cross sections of the annular intensity profiles of the PVBs along the vertical direction with topological charges  $l = 1, 2, 3,$  and  $4$  at wavelengths of  $450 \text{ nm}$  (a-d) and  $630 \text{ nm}$  (e-h).

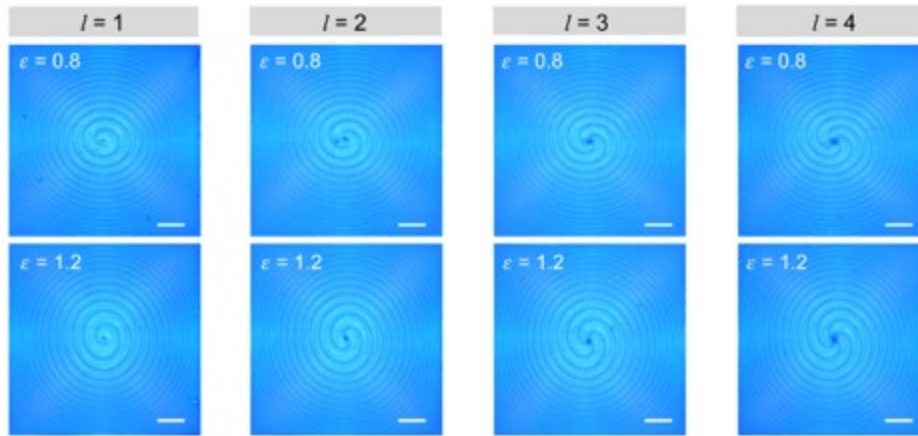


**Figure S5** Optical microscope images of the fabricated metasurfaces ( $\epsilon = 0.8$ ,  $\epsilon = 1.2$ ) with topological charges of  $l = 1, 2, 3$ , and  $4$  (from left to right). Scale bar:  $10 \mu\text{m}$ .

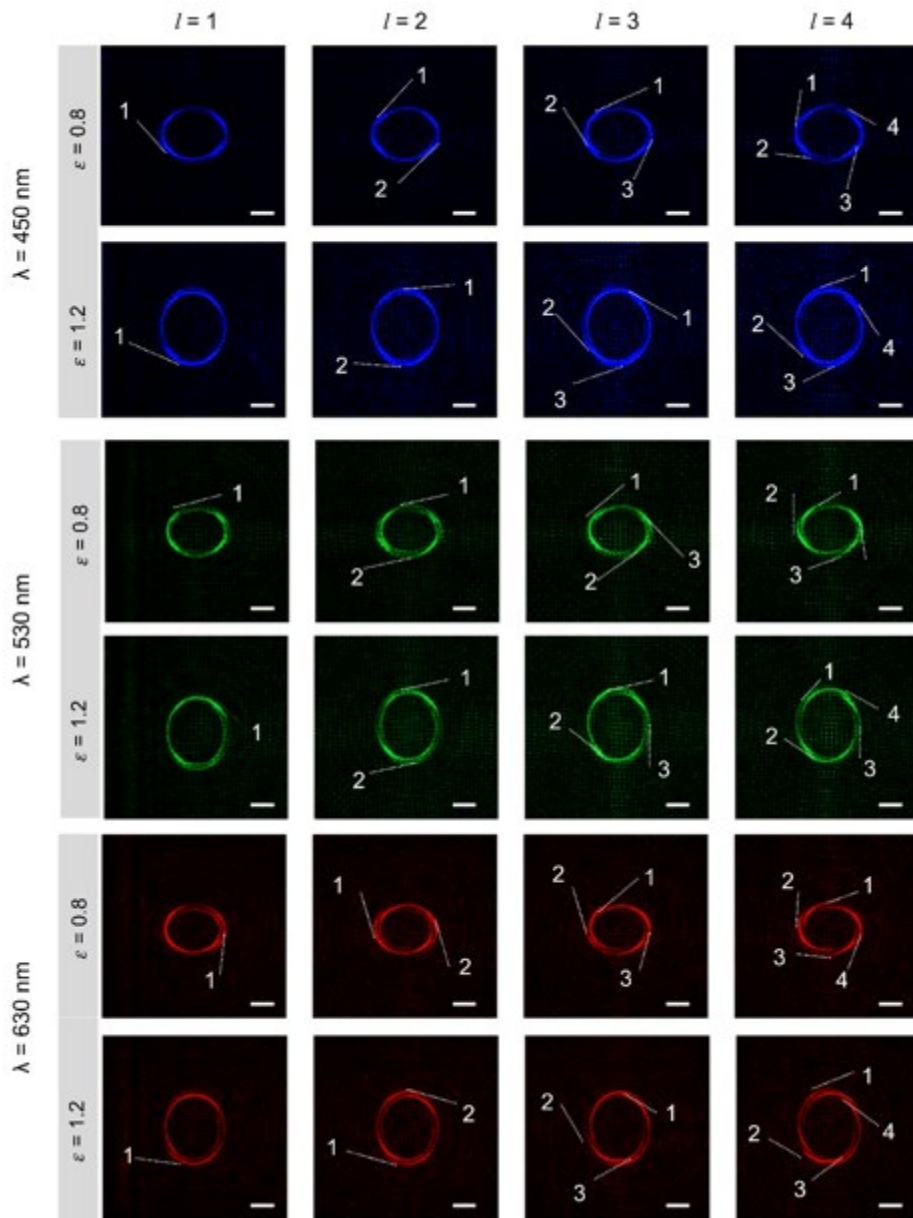


**Figure S6** The measured interference patterns corresponding to the PVBs ( $\epsilon = 0.8$ ,  $\epsilon = 1.2$ ) generated by the metasurface:  $NA = 0.08$ . Scale bar:  $10 \mu\text{m}$ .

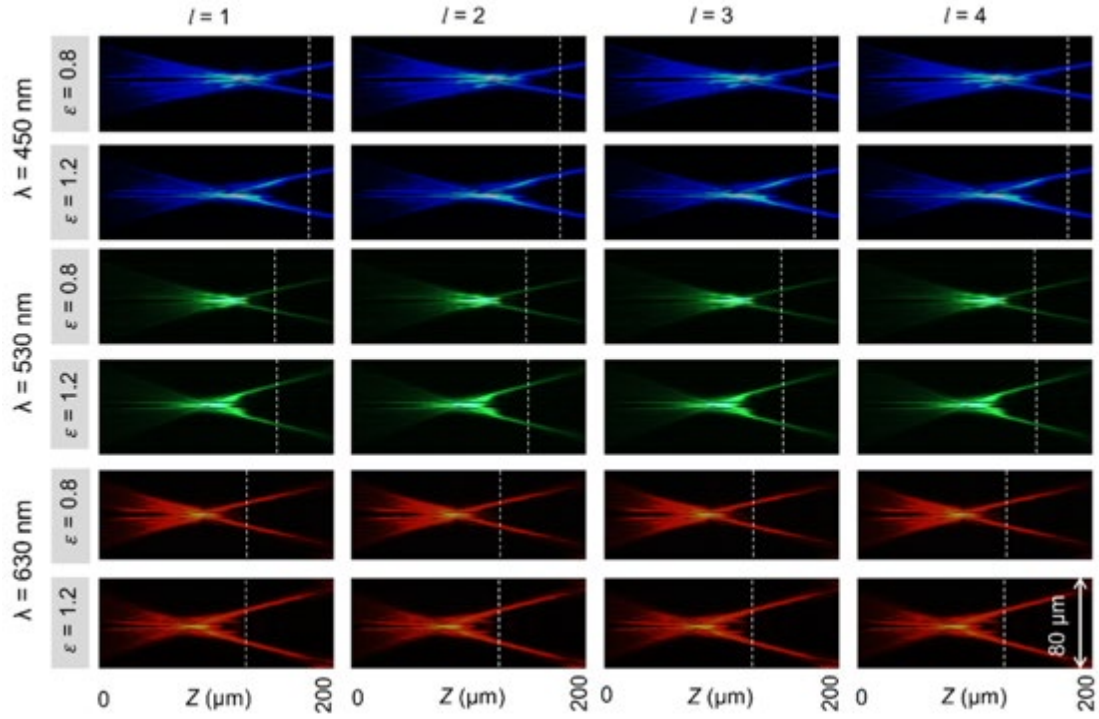


**Figure S7** The  $y$ - $z$  plane intensity distributions of the vortex beams ( $\varepsilon = 0.8$ ,  $\varepsilon = 1.2$ ) using the metasurface:  $NA = 0.08$ . The propagation distances represented by the white dotted line at the three wavelengths are  $z = 180 \mu\text{m}$ ,  $150 \mu\text{m}$ , and  $128 \mu\text{m}$ .

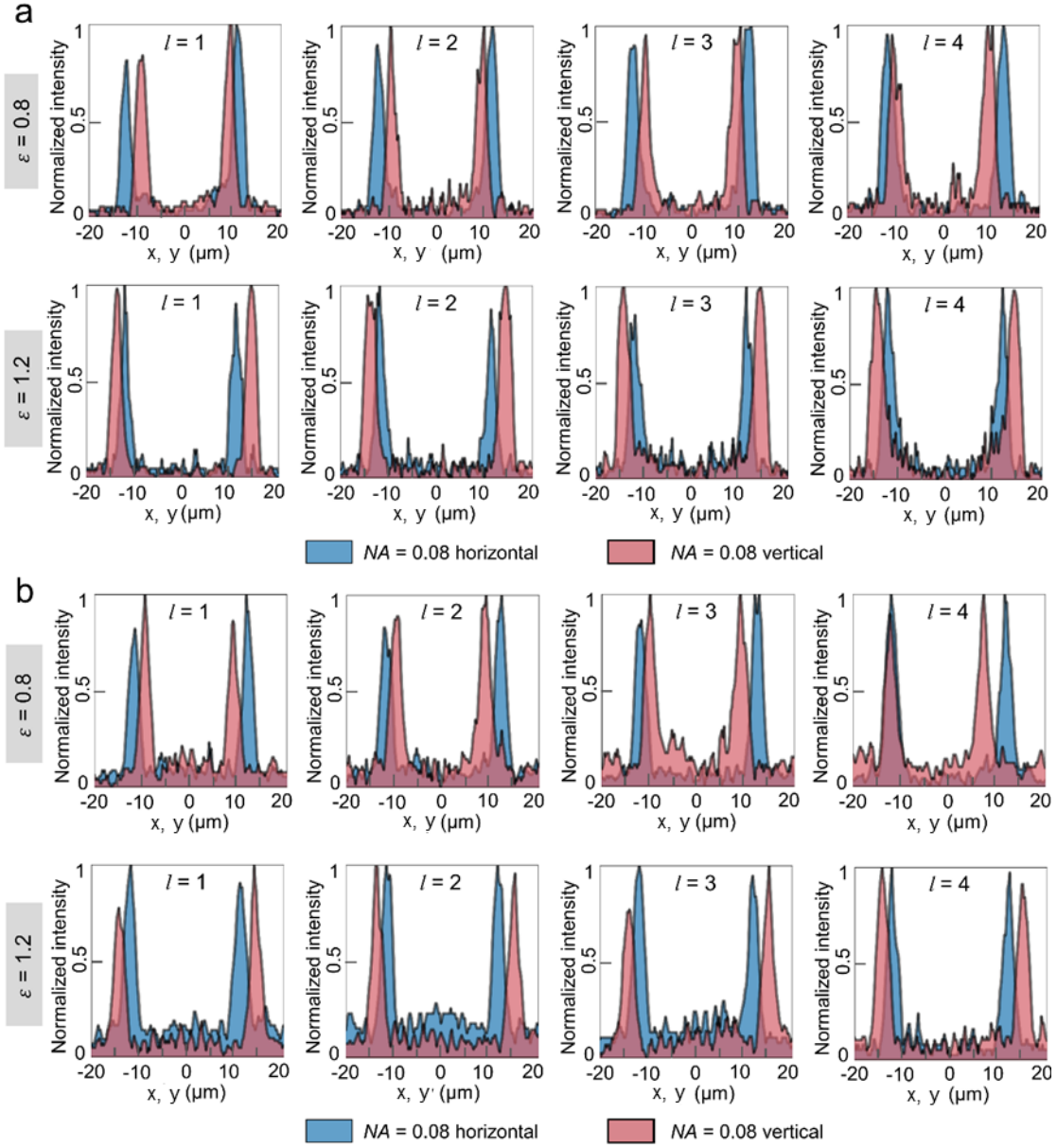


**Figure S8** Normalized cross-sections of the annular intensity profiles of the PVBs ( $\epsilon = 0.8$ ,  $\epsilon = 1.2$ ) generated by the metasurface:  $NA = 0.08$  indicated by the filled area with topological charges  $l = 1, 2, 3$ , and  $4$  at the wavelength of (a)  $450$  nm and (b)  $630$  nm.

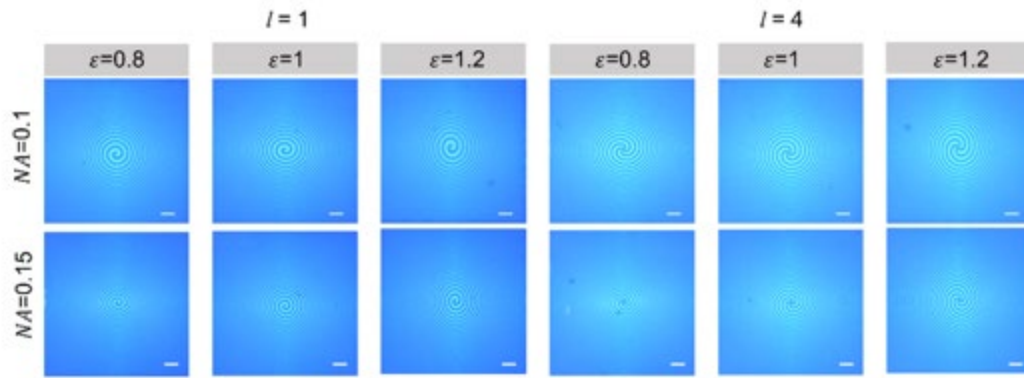


**Figure S9** Optical microscope images of the fabricated metasurfaces ( $\epsilon = 0.8$ ,  $\epsilon = 1$ . and  $\epsilon = 1.2$ ) with topological charges of  $l = 1$  and  $4$  ( $NA = 0.1$  and  $NA = 0.15$ ). Scale bar:  $10 \mu\text{m}$ .

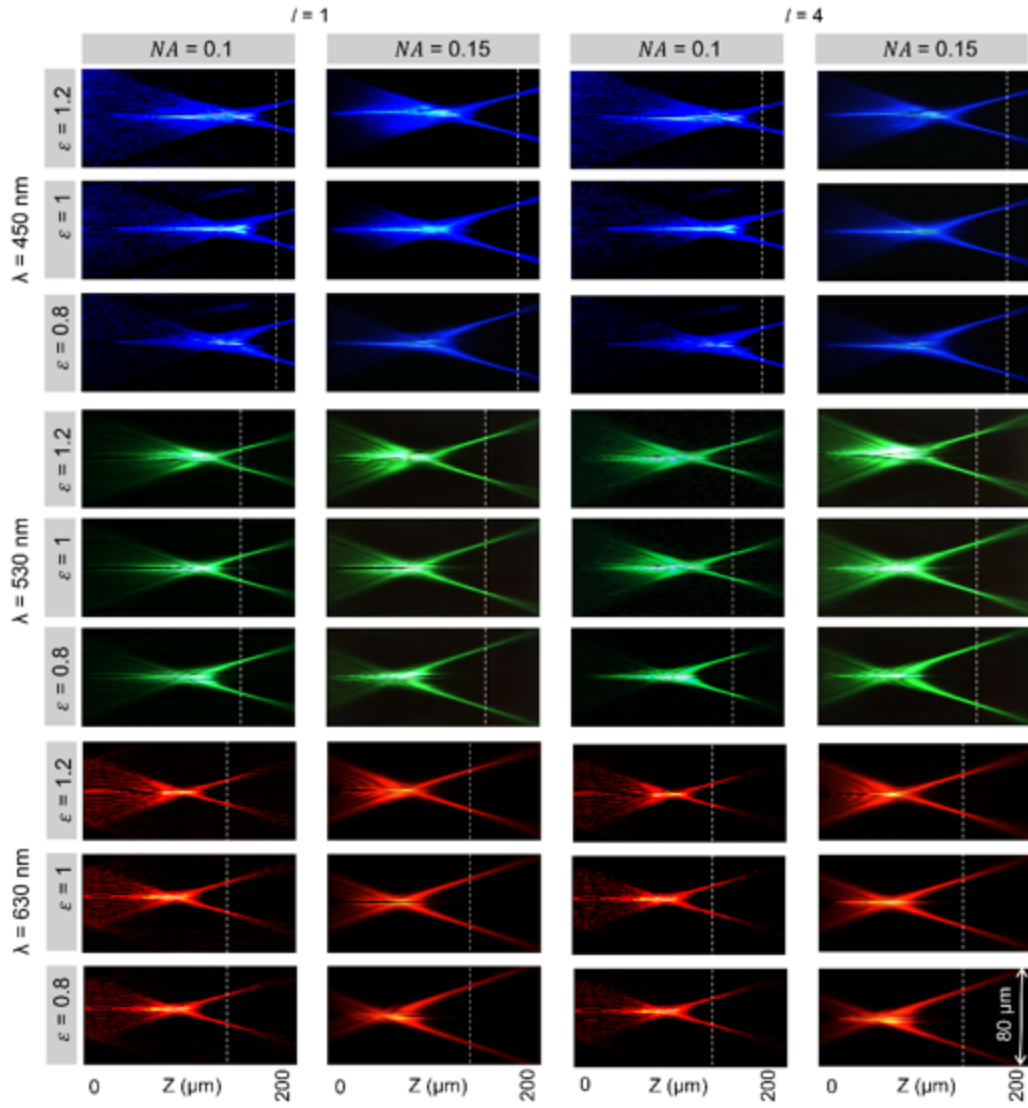


**Figure S10** The  $y$ - $z$  plane intensity distributions of the vortex beams ( $\varepsilon = 0.8$ ,  $\varepsilon = 1$ , and  $\varepsilon = 1.2$ ) using the metasurface:  $NA = 0.1$  and  $NA = 0.15$ . The propagation distances represented by the white dotted line at the three wavelengths are  $z = 180 \mu\text{m}$ ,  $150 \mu\text{m}$ , and  $128 \mu\text{m}$ , respectively.

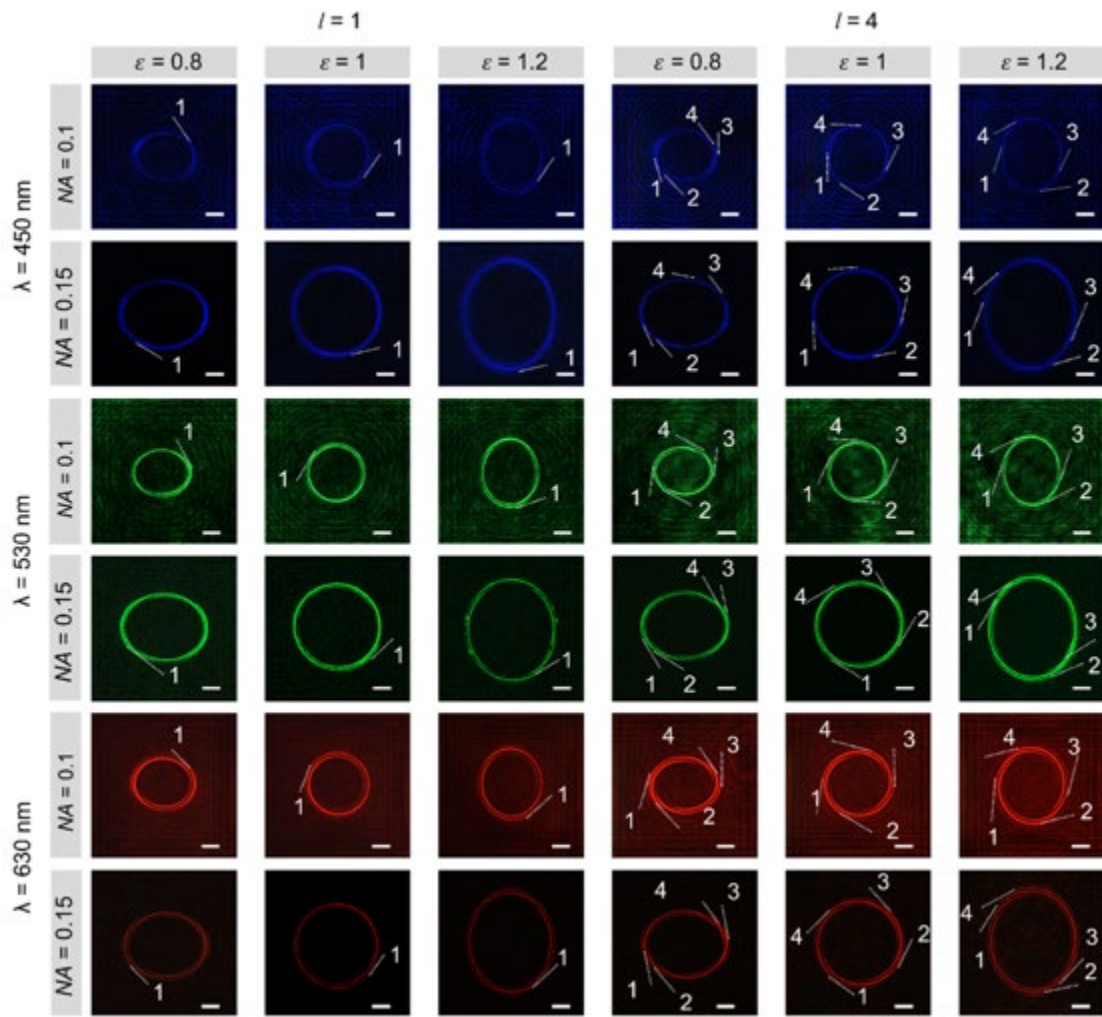


**Figure S11** The measured interference patterns corresponding to the PVBs ( $\epsilon = 0.8$ ,  $\epsilon = 1$ , and  $\epsilon = 1.2$ ) generated by the metasurface:  $NA = 0.1$  and  $NA = 0.15$ . Scale bar:  $10 \mu\text{m}$ .

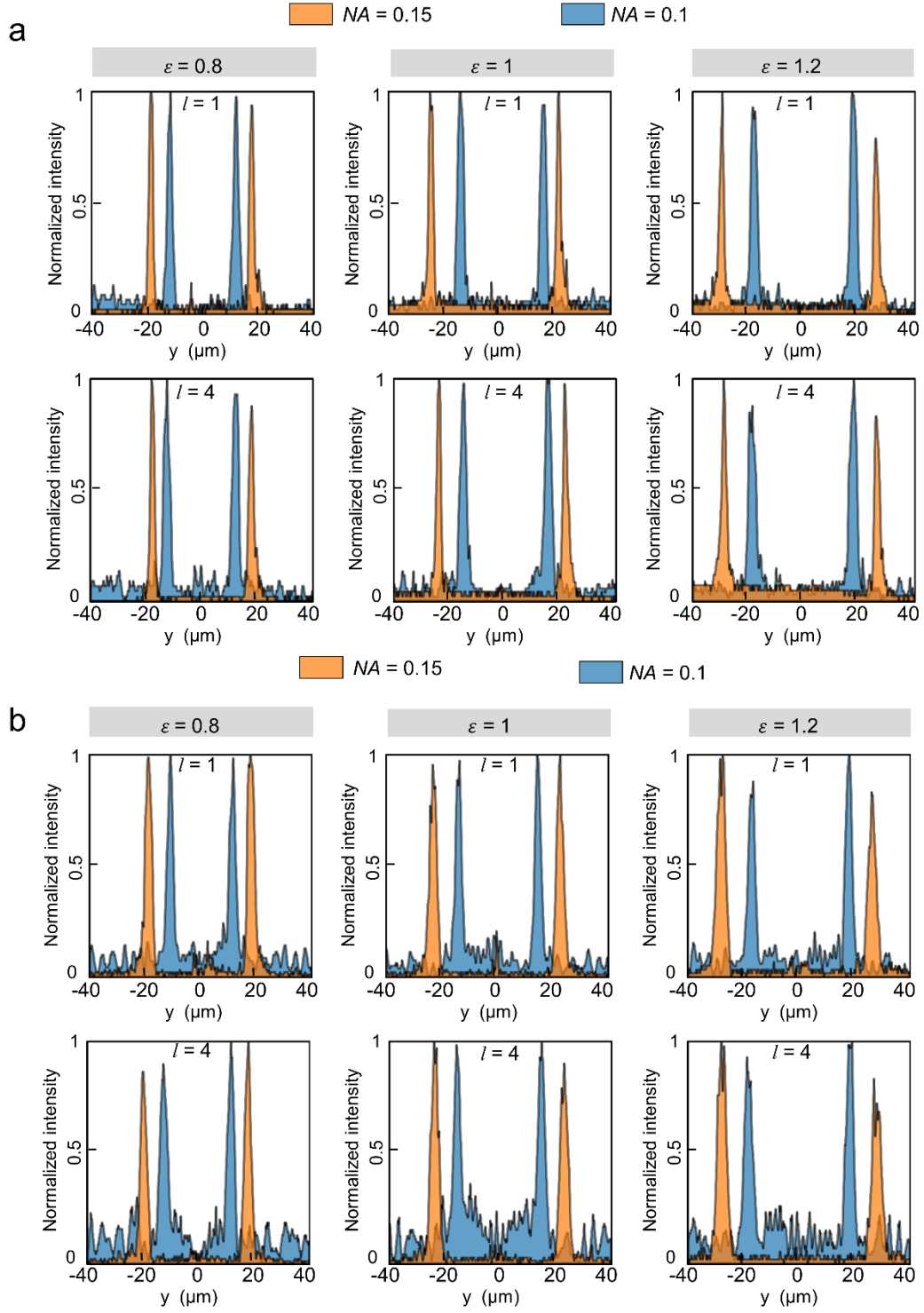


**Figure S12** Normalized cross-sections (the vertical direction) of the annular intensity profiles of the PVBs with topological charges  $l = 1$  and  $4$  at the wavelength of (a) 450 nm and (b) 630 nm.

**Table S1** The measured and theoretical value of PVB's diameter ( $\varepsilon = 0.8$ ,  $\varepsilon = 1$  and  $\varepsilon = 1.2$ ) using the fabricated metasurfaces with  $NA = 0.1$  (a) and  $0.15$  (b). The uncertainties in diameter measurements are one standard deviation of the Gaussian fit parameter.

Metasurface with $NA = 0.1$					
		$l = 1$		$l = 4$	
		Horizontal diameter/ $\mu\text{m}$	Vertical diameter/ $\mu\text{m}$	Horizontal diameter/ $\mu\text{m}$	Vertical diameter/ $\mu\text{m}$
$\varepsilon = 0.8$	Measured value	$30.15 \pm 0.13$	$25.58 \pm 0.08$	$31.02 \pm 0.11$	$25.78 \pm 0.07$
	Theoretical value	30	24	30	24
$\varepsilon = 1$	Measured value	$30.07 \pm 0.10$	$31.87 \pm 0.11$	$30.09 \pm 0.09$	$31.47 \pm 0.08$
	Theoretical value	30	30	30	30
$\varepsilon = 1.2$	Measured value	$30.07 \pm 0.05$	$36.95 \pm 0.06$	$30.54 \pm 0.07$	$36.81 \pm 0.05$
	Theoretical value	30	36	30	36

**b**

Metasurface with $NA = 0.15$					
		$l = 1$		$l = 4$	
		Horizontal diameter/ $\mu\text{m}$	Vertical diameter/ $\mu\text{m}$	Horizontal diameter/ $\mu\text{m}$	Vertical diameter/ $\mu\text{m}$
$\varepsilon = 0.8$	Measured value	$46.00 \pm 0.12$	$36.95 \pm 0.13$	$46.01 \pm 0.13$	$37.15 \pm 0.15$
	Theoretical value	45	36	45	36
$\varepsilon = 1$	Measured value	$45.17 \pm 0.11$	$46.09 \pm 0.13$	$45.19 \pm 0.09$	$46.09 \pm 0.09$
	Theoretical value	45	45	45	45
$\varepsilon = 1.2$	Measured value	$45.55 \pm 0.09$	$54.62 \pm 0.12$	$45.37 \pm 0.11$	$54.52 \pm 0.09$
	Theoretical value	45	54	45	54